

Variational Transition State Theory and Tunneling Calculations with Reorientation of the Generalized Transition States for Methyl Cation Transfer

Angels González-Lafont, Jordi Villà, José M. Lluch,* and Juan Bertrán

Department de Química, Universitat Autònoma de Barcelona, 08193 Bellaterra, Barcelona, Spain

Rozeanne Steckler

Sand Diego Supercomputer Center, P.O. Box 85608, San Diego, California 92186-9784

Donald G. Truhlar*

Department of Chemistry and Supercomputer Institute, University of Minnesota, Minneapolis, Minnesota 55455-0431

Received: January 13, 1998

The new RODS algorithm based on optimizing the orientation of the dividing surface at each point along the reaction path in order to maximize the free energy of the generalized transition state containing that point has been used to carry out variational transition state calculations and tunneling calculations for two reactions with high-frequency vibrations strongly coupled to the reaction coordinate, $(\text{Cl}^-)(\text{CH}_3\text{NH}_3^+) \rightarrow \text{ClCH}_3(\text{NH}_3)$ and $\text{ClCH}_3 + \text{NH}_3$, and $\text{CH}_3\text{Cl}(\text{H}_2\text{O}) + \text{NH}_3(\text{H}_2\text{O}) \rightarrow (\text{CH}_3\text{NH}_3^+)(\text{Cl}^-)(\text{H}_2\text{O})_2$. These reactions, both of which involve the transfer of a methyl cation between Cl^- and NH_3 , show much larger variational-transition-state and tunneling effects than were observed in previous studies of the transfer of methyl cations between anionic centers. However, they are hard to study because the adiabatic potential energy curves of both reactions and, as a consequence, the corresponding free energy of activation profiles show big dips when the minimum energy path (MEP) is followed using standard methods, even when very small step sizes are taken to compute the steepest-descent path. The application of RODS methodology eliminates those dips, giving rise to smooth free energy of activation profiles and vibrationally adiabatic potential curves. Calculations of variational rate constants and tunneling effects are significantly improved.

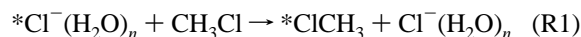
1. Introduction

The fundamental hypothesis of conventional transition state theory (TST) is that, in terms of classical mechanics, no trajectories in an equilibrium ensemble recross a transition-state dividing surface (a hypersurface dividing reactants from products) centered at the saddle point on a potential energy hypersurface.¹ Because of this assumption, TST in a classical world overestimates the thermal rate constants of chemical reactions.^{1,2} Variational transition state theory (VTST) minimizes this error by locating the transition-state dividing surface such that it yields the smallest possible calculated rate constant. It can be shown that this maximizes the free energy of activation.^{3,4} In practice, one adds quantum mechanical effects on modes transverse to the reaction coordinate by computing the free energy of activation from quantum mechanical sums over states rather than classical phase space integrals.^{5,6} This must be justified by the existence of locally conserved vibrational action variables that are seen to be clearly quantized in accurate quantum mechanical calculations; these are the locally adiabatic invariants of the motion.⁷

Prior to calculating the VTST rate constants, one must compute generalized frequencies along the path in order to get the free energy of activation profile. VTST calculations based on a search along the minimum-energy path (MEP) for the best location of the transition state have the drawback that they can be very expensive to calculate the MEP, because small step

sizes are required to accurately compute an MEP.⁸ Furthermore, if the MEP is not accurate, the generalized normal mode frequencies corresponding to the usual dividing surface normal to the path may be unphysical and differ greatly from the true locally adiabatic invariants. In a previous paper⁹ a new practical method for carrying out VTST calculations without evaluating the MEP has been presented. In this method, for each point along a reaction path (which is not necessarily the minimum-energy path), the orientation of the dividing surface is optimized in order to maximize the free energy of the generalized transition state at that point. Another use of the proposed algorithm is that it can be employed to extract a stable and meaningful free energy of activation from an MEP-based calculation carried out with large steps, where the usual procedure of orienting the dividing surface normal to the gradient of the potential is inaccurate.

During the past two decades, VTST has been applied to a variety of chemical systems.¹⁰ A wide variety of reactions of neutral species have been studied, with variational effects of various magnitudes.¹⁰ Among ionic reactions, much attention has been devoted to bimolecular ion–neutral reactions of the $\text{S}_{\text{N}}2$ and $\text{E}2$ type. In particular, considerable attention has been dedicated to ion–molecule $\text{S}_{\text{N}}2$ reactions such as^{11–15}



with $n = 0, 1$, or 2 . It has been found for all ion–molecule

S_N2 reactions studied so far that variational effects (by which we mean deviations of VTST predictions from TST ones) are very small both for the transition-state location and for the determination of the corresponding rate constant.^{11–18} For instance, calculations based on a semiempirical, analytical potential energy hypersurface indicate that the VTST rate constant for reaction R1 is within 1% of the TST result at 300 K for $n = 0$ and 1.¹⁵ These results may be attributed to the facts that (i) as the system leaves the saddle point along the reaction path, the energy tends to drop rapidly to negative values associated with ion–dipole complexes, and (ii) the vibrational frequencies change only slowly along the reaction path in the vicinity of the saddle point. One E2 reaction has been studied, namely,

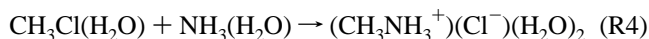


Variational effects on the reaction rate in the central barrier were found to be only about 4%.¹⁸

However, variational effects on reaction rates for S_N2 reactions need not always be small. In this paper we present a study of two reactions that show significant variational effects. These systems are difficult to study because the vibrationally adiabatic potential energy curves and the corresponding free energy of activation curves have significant dips when the MEP is followed using standard methods. We will show that the application of the above mentioned new algorithm based on the reorientation of the dividing surface (which will be called RODS) eliminates the dips, giving rise to smooth free energy of activation curves. In the original paper on the RODS algorithm, three examples were used to validate the new methodology. The present paper applies the RODS algorithm for complete VTST calculations of more difficult cases involving strong coupling of high-frequency modes to the reaction coordinate. In particular, we study

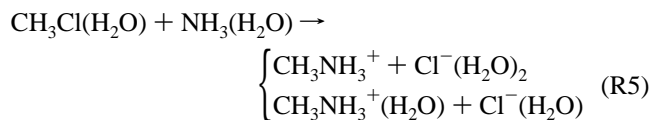


and



The presence of microsolvating water molecules in R4 makes the calculation of free energy of activation curves even less stable than for the base case. Note that the unimolecular reaction R3 can produce either a van der Waals complex or a pair of separated neutral products; the exoergicities of these two paths are 30.5 and 28.9 kcal/mol, respectively. Note, however, that both paths go through the same transition state so transition state theory can predict only the sum of the two rates. Reaction R4 is a bimolecular reaction that produces a dihydrated ion pair; the exoergicity of this reaction is 20.7 kcal/mol. For both R3 and R4 we consider the gas-phase high-pressure plateau. Thus we consider that collisions are frequent enough to maintain an equilibrium distribution of reactant energies for R3 and to stabilize all products of both R3 and R4. We assume, however, that the pressure is not so extraordinarily high that collisions of bath molecules with the transition states would need to be considered.

Reaction R4 is closely related to the Menshutkin reaction, which has been widely studied.¹⁹ The Menshutkin analog of R4 is



which is about 85 kcal/mol endoergic. Whereas the dynamical bottleneck for R5 occurs during the dissociation of the product-like ion pair, the rates of reactions R3 and R4 are both determined by central transition states corresponding to transfer of CH_3^+ . However, as compared to ion–molecule S_N2 reaction studied previously, the CH_3^+ transfer steps in R3 and R4 are between a charged and a neutral fragment rather than between two charged fragments.

In order to calculate reaction rates by variational transition state theory, potential energy information is required at the stationary points and along the reaction path. For the present studies this information is obtained directly from electronic structure calculations without the intermediacy of an analytic fit; that is, we carry out “direct dynamics VTST”.^{13–17,20–23} By design, the application of RODS methodology does not require any additional electronic structure calculation.

Section 2 presents the details of the electronic structure calculations and dynamical calculations. Section 3 presents the results, and section 4 is the discussion. Section 5 summarizes the principal conclusions.

2. Computational Methods

2.1. Electronic Structure. As our main purposes of this work are to explore qualitative features of new reaction types and to illustrate new methodology, it is not essential to include electron correlation energy. Ab initio restricted Hartree–Fock calculations²⁴ were carried out using the split valence 6-31+G-(d) basis set,²⁵ which includes d polarization and diffuse functions on the heavy atoms. Full geometry optimization was carried out. Stationary points were characterized as minima or saddle points by diagonalizing their Hessian (force constant) matrices and confirming that there are zero or one negative eigenvalue, respectively.

The minimum-energy path (MEP) was calculated in mass-scaled Cartesian coordinates^{26,27} with a reduced mass, μ , of 1 amu by using the fourth-order Runge–Kutta method²¹ with a variable step size. For R3 a maximum value of 0.0026 Å was employed within the interval (–0.1 Å, 0.1 Å) of the MEP. Beyond this interval, the maximum was 0.0079 Å. For R4, the corresponding values were 0.0052 and 0.013 Å, respectively, within the same intervals. Analytic Hessians were calculated at selected points along the MEP, with the convergence criterion explained in the following section. After diagonalizing the projected Hessian³⁰ at each point on the MEP, we obtain the m (where $m = 1, 2, \dots, 3N-7$, and N is the number of atoms) generalized normal-mode frequencies corresponding to the modes orthogonal to the MEP (which are ordered in decreasing order), which allow us to calculate the vibrationally adiabatic ground-state potential curve $V_a^G(s)$. This is defined by

$$V_a^G(s) = V_{\text{MEP}}(s) + \text{ZPE}(s) \quad (1)$$

where s denotes distance along the MEP in the mass-scaled system.²⁷ The eigenvectors \mathbf{L}_m obtained from the diagonalization, along with the gradient \mathbf{v} at the points on the MEP, are used to compute $B_{mF}(s)$, the reaction-path curvature at each mode m , in the usual way.^{27,30}

$$B_{mF}(s) = -[\text{sign}(s)] \sum_{i=1}^{3N} \frac{dv_i(s)}{ds} L_{i,m}^{\text{GT}}(s) \quad (2)$$

Partial charges on the atoms and groups (q_X and q_{XH_n} , respectively, where X and H denote atoms) were calculated for interpretive purposes (they are not required for gas-phase dynamics calculations) by the method of Mulliken population analysis.²⁸ For the final results, all electronic structure calculations were done using the GAMESS93 electronic structure code.²⁹

2.2. Dynamics. *2.2.1. Theory.* Rate constants are calculated by canonical variational theory (CVT).²⁷ This theory yields hybrid rate constants corresponding to classical reaction path motion with other degrees of freedom quantized. However, since the rotational energy levels are generally closely spaced, we approximate the quantal rotational partition functions by the classical ones. For vibrations, the partition functions were calculated quantum mechanically within the harmonic approximation in rectilinear coordinates.^{3,27,30}

To include quantal tunneling effects for motion along the reaction coordinate, CVT rate constants were multiplied by a ground-state transmission coefficient.^{4,6,14,27,31,32} In particular we employ zero-curvature tunneling^{5,6,26} (ZCT) and the centrifugal-dominant small-curvature semiclassical adiabatic ground-state^{31,32} (small-curvature tunneling or SCT) approximations. The ZCT method corresponds to tunneling along the MEP, and the SCT method allows corner cutting in the tunneling probabilities.

2.2.2. Grids. The potential energy information (energies, gradients, and Hessians), calculated at selected points along the MEP, was used in a modified version of the POLYRATE computer code, version 7.0,^{31,33} in order to carry out direct dynamics studies of processes R3 and R4. To assure convergence of the calculated rate constants, preliminary rate calculations with coarse Hessian grids were used to locate the regions of the reaction path containing the temperature-dependent variational transition states and the minima of the SCT reduced mass, where the “corner cutting” aspect of the tunneling process would be greatest. Finer grids were then calculated for these critical regions to improve the accuracy of the calculated canonical rate constants and small-curvature tunneling probabilities. This strategy is sometimes called focusing.²³ A total of 79 and 67 Hessian grid points were finally used for reactions R3 and R4, respectively.

The potential energy and generalized-normal-mode vibrational frequencies were then interpolated to intervals of 0.0026 Å by five-point Lagrangian interpolation. Both diabatic³⁴ and adiabatic correlations of frequencies along the MEP were carried out (for the diabatic correlation a new methodology implemented in one of our programs³⁵ was used). The reaction-path curvature components at each step were evaluated by POLYRATE from the corresponding generalized-normal-mode eigenvectors and the derivatives of the gradient vectors.²⁷

2.2.3. Reorientation of the Dividing Surface (RODS). In the RODS algorithm we assume that a Taylor series of the potential, valid through quadratic terms, is available for each of a series of K points along a generic reaction path, which is not necessarily the MEP. We specify these points as $k = 1, 2, \dots, K$ and let \mathbf{x} denote our mass-scaled Cartesian³⁶ coordinate system. Let $\mathbf{x}^L(k)$ denote the K points where the data are available. Generally, the dividing surfaces, which are hyperplanes in \mathbf{x} passing through the different $\mathbf{x}^L(k)$, are obtained by projecting the gradient and the overall translations and rotations out of the Hessian matrix.³⁰ In the RODS approach, we will

consider trial dividing surfaces that are orthogonal to the overall rotations and translations and that pass through one of the points $\mathbf{x}^L(k)$. However, instead of projecting out the gradient, for each k we optimize the orientation of the dividing surface to maximize the generalized free energy of activation of the generalized transition state at k . In this way we obtain more physical dividing surfaces especially when the calculations are unstable. Details of the algorithm are given elsewhere,⁹ but we note that s is still calculated by the fourth-order Runge–Kutta algorithm even though the RODS algorithm slightly displaces the points on the reaction path.

3. Results and Discussion

3.1. Stationary Points. Tables 1 and 2 give the energy, relative to reactants, at stationary points along the MEP for reactions R3 and R4; this quantity is labeled V_{MEP} . Tables 1 and 2 also give geometrical parameters and partial charges characterizing the stationary points. Both reactions can be visualized as the transfer of a CH_3^+ group between Cl^- and NH_3 , accompanied by the umbrella inversion at CH_3^+ .

For reaction R3, the Cl, C, and N atoms are collinear along the entire minimum-energy reaction path. The saddle point is depicted in Figure 1, along with the imaginary frequency eigenvector. One can observe that the main components of the transition vector (whose eigenvalue gives an imaginary frequency of 559i cm^{-1}) correspond to the nitrogen atom separating from the carbon atom. Therefore, the reaction coordinate is fundamentally an asymmetric stretch at the conventional transition state. The neutralization of the chloride charge progresses monotonically along the reaction path.

For the dihydrated reaction R4, the general effect of solvent is to stabilize the supermolecule as the reaction progresses, which is why this reaction would probably be studied experimentally in the ion production direction, as written, rather than in neutralization direction, as R3 is written. The dipole–dipole complex is 5.1 kcal/mol below the reactants, and the energy barrier referred to this complex is 25.6 kcal/mol. The product ion–pair complex is stabilized by the hydrating water molecules in such a way that it appears 15.6 kcal/mol below the dipole–dipole complex.

Some aspects of the geometrical structures merit discussion. At the reactants, one water molecule, called W(N), is hydrogen bonded to one of the ammonia hydrogens, while the second water molecule, called W(Cl), solvates the chlorine atom. As the reaction proceeds, an interesting motion of the different fragments takes place to stabilize the nascent charges. Initially the reactants approach with nonlinear Cl–C–N arrangement to give the dipole–dipole complex shown in Figure 2, in such a way that the two water molecules are able to form a hydrogen bond between them. In addition, the W(Cl) water molecule continues to solvate the chlorine atom, and the W(N) water molecule continues to solvate the ammonia. At the saddle point, shown in Figure 3, the nitrogen, carbon, and chlorine atoms are aligned. The N–C distance is short enough that both water molecules still remain hydrogen-bonded to each other. We note that the transition vector is very similar to the one associated with the unhydrated reaction, such that no significant component of motion of water molecules appears. Thus, the imaginary frequency (551i cm^{-1}) has an only slightly lower value than for the R3 reaction. At the ion-pair product, shown in Figure 4, W(N) maintains the same interaction as at the saddle point; that is, it solvates ammonia and is hydrogen-bonded to W(Cl); whereas W(Cl) solvates the chloride anion. The methyl group appears completely unsolvated. This structure is reasonable in

TABLE 1: Stationary Point Energies, Geometries, and Partial Charges for Reaction R3

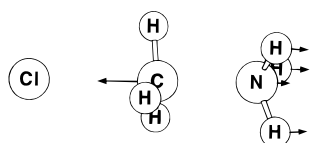
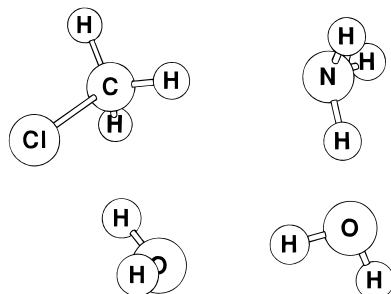
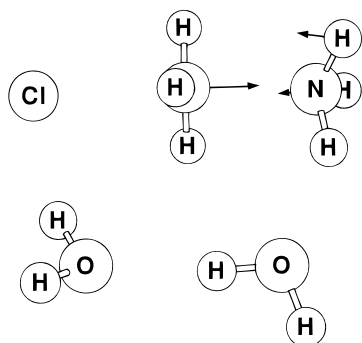
species	V_{MEP} (kcal/mol)	$R(\text{C}-\text{N})$ (Å)	$R(\text{C}-\text{Cl})$ (Å)	$\theta(\text{H}-\text{C}-\text{N})$ deg	$\theta(\text{C}-\text{N}-\text{H})$ (deg)	q_{CH_3} (au)	q_{NH_3} (au)	q_{Cl} (au)
$(\text{Cl}^-)(\text{CH}_3\text{NH}_3^+)$	0.0	1.541	2.918	107.9	111.2	0.46	0.43	-0.89
saddle point	7.2	1.900	2.474	96.1	111.1	0.49	0.21	-0.70
$\text{ClCH}_3(\text{NH}_3)^a$	-30.5	3.533	1.793	71.5	111.1	0.12	-0.01	-0.11
$\text{ClCH}_3 + \text{NH}_3$	-28.9	∞	1.786			0.06	0.00	-0.06

^a Dipole-dipole complex.

TABLE 2: Stationary Point Energies, Geometries, and Partial Charges for Reaction R4

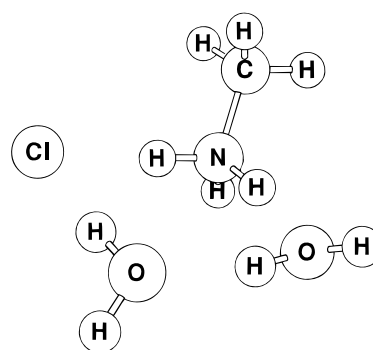
species	V_{MEP} (kcal/mol)	$R(\text{C}-\text{N})$ (Å)	$R(\text{C}-\text{Cl})$ (Å)	$R(\text{N}-\text{Cl})$ (Å)	$R(\text{Cl}-\text{H})^a$	$R(\text{N}-\text{O})^b$ (Å)	q_{CH_3} (au)	q_{NH_3} (au)	q_{Cl} (au)	$q_{\text{W}(\text{Cl})}$ (au)	$q_{\text{W}(\text{N})}$ (au)
$\text{CH}_3\text{Cl}(\text{H}_2\text{O}) + \text{NH}_3(\text{H}_2\text{O})$	0.0	∞	1.79	∞	2.84	3.04	0.11	-0.02	-0.10	0.00	0.02
$\text{CH}_3\text{Cl}(\text{H}_2\text{O})[\text{NH}_3(\text{H}_2\text{O})]^c$	-5.1	3.58	1.80	4.58	2.64	3.20	0.14	-0.01	-0.12	-0.02	0.01
saddle point	20.5	2.04	2.38	4.41	2.34	2.99	0.51	0.16	-0.63	-0.04	0.01
$(\text{CH}_3\text{NH}_3^+)(\text{Cl}^-)(\text{H}_2\text{O})_2$	-20.7	1.48	3.74	3.02	2.32	2.86	0.30	0.51	-0.78	-0.04	0.01

^a $R(\text{Cl}-\text{H})$ is the distance from Cl to the closest water H atom, and $q_{\text{W}(\text{Cl})}$ is the partial charge on the water hydrogen that is bonded to Cl. ^b $R(\text{N}-\text{O})$ is the distance from N to the closest water O atom, and $q_{\text{W}(\text{N})}$ is the partial charge on the water hydrogen that is bonded to N. ^c Dipole-dipole complex.

**Figure 1.** Saddle point of the unhydrated reaction R3 along with components of the transition vector in mass-scaled Cartesian coordinates.**Figure 2.** Dipole-dipole complex of the dihydrated reaction R4.**Figure 3.** Saddle point of the dihydrated reaction R4 along with the main components of the transition vector in mass-scaled Cartesian coordinates.

a dihydrated cluster where the chloride anion prefers to be bonded to the most positive fragment of the supermolecule. This combination of stabilizing interactions causes the ion-pair product to lie in a deep well.

3.2. VTST Calculations Based on the Standard Algorithm. **3.2.1. Runge-Kutta Calculations.** The position of the variational transition state corresponds to the maximum of the free energy of activation profile at each temperature. At 0 K that profile equals the vibrationally adiabatic ground-state potential energy curve defined by eq 1. Solid lines in Figure

**Figure 4.** Ion-pair product of the dihydrated reaction R4.

5a,b show the adiabatic ground-state potential energy curves for reactions R3 and R4, respectively. To show the effect of temperature, the solid lines in Figure 6a,b present the free energy of activation profiles at $T = 300$ K for these reactions. The shapes of the profiles at the other temperatures considered are similar to their shapes at 300 K. We note in Figure 5a,b important dips appearing in the region near the saddle point, which is the region that apparently governs the variational effects. In order to analyze the regions of these dips, we next examine the vibrational frequencies in these regions.

Figures 7 and 8 present the generalized-normal-mode vibrational frequencies of the high-frequency generalized normal modes versus the arc length along the reaction coordinate for reactions R3 and R4, respectively. Note that the mode of $(\text{Cl}^-)(\text{CH}_3\text{NH}_3^+)$ correlating with the imaginary normal mode at the saddle point is not included because it is the reaction coordinate. The generalized normal modes shown in these two figures exhibit strong couplings at various points along the reaction path. For that reason, we have preferred to make a diabatic correlation in Figures 7 and 8. For the sake of simplicity, only the generalized normal modes associated with reactant frequencies above 1500 cm^{-1} are displayed.

In the unhydrated reaction R3, only one frequency changes significantly in the vicinity of the saddle point. This generalized-normal-mode frequency takes values of around 3800 cm^{-1} along the incoming part of reaction path and decreases abruptly just before the saddle point, where it reaches a local maximum of 3813 cm^{-1} . Another dip occurs on the product side of the MEP. The analysis of the associated generalized-normal-mode eigenvector along the reaction path shows that this mode corresponds to a vibrational motion of the ammonia hydrogen atoms in the 3800 cm^{-1} region. The two dips of this frequency

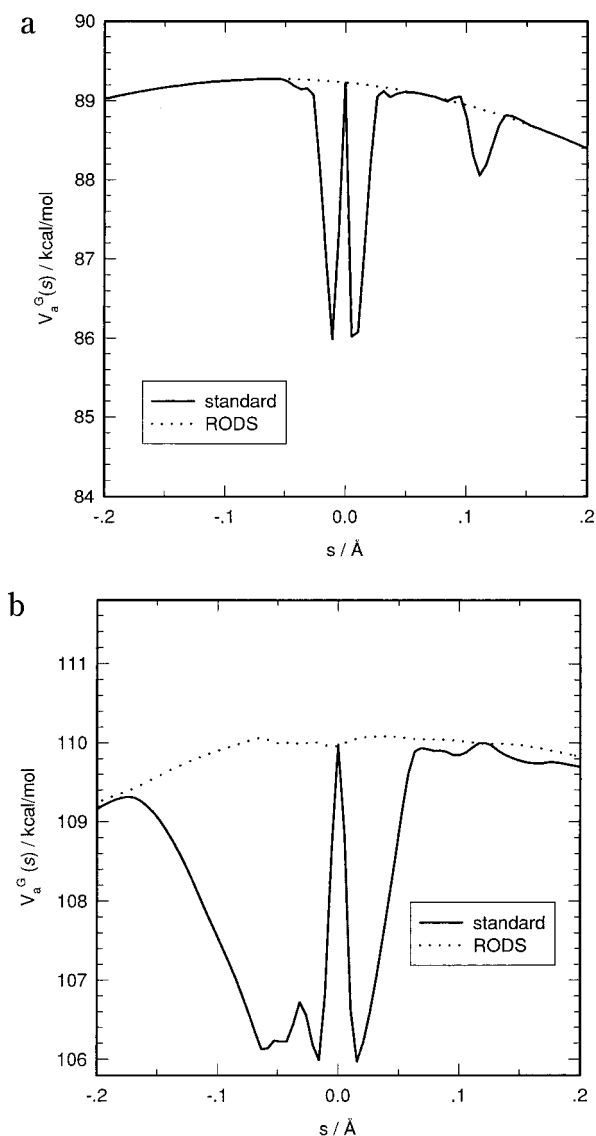


Figure 5. Detail of the adiabatic ground-state potential energy curves (in kcal mol⁻¹) versus the arc length along the reaction coordinate (in Å) for reactions R3 (a) and R4 (b). Solid lines correspond to the standard VTST calculation. Dotted lines correspond to the RODS VTST calculation.

just before and after the saddle point are explained by a strong mode coupling that changes the components of the generalized-normal-mode eigenvector which in those two zones correspond to the motion of the ammonia hydrogen atoms plus the motion of the nitrogen atom separating from the carbon atom. As a consequence of the variation of this frequency, the total zero-point energy goes down rapidly just before and after the saddle point, as seen in Figure 5a.

For the dihydrated reaction R4, there are two frequencies, labeled A and B in Figure 8, that change significantly in the vicinity of the saddle point. For the frequency A three zones can be distinguished. Coming from reactants, frequency A takes values above 4000 cm⁻¹. Just before the saddle point it drops abruptly below 1500 cm⁻¹. Finally, just after the saddle point, where it has a value of 3659 cm⁻¹, up to products it remains nearly constant. In the first zone, the associated generalized-normal-mode eigenvector involves primarily the movement of the water hydrogen atoms. In the second zone, when the frequency goes down, the normal mode consists of the motion of the ammonia and W(N) water hydrogen atoms plus the N–C stretching (the incorporation of these two heavy atoms causes

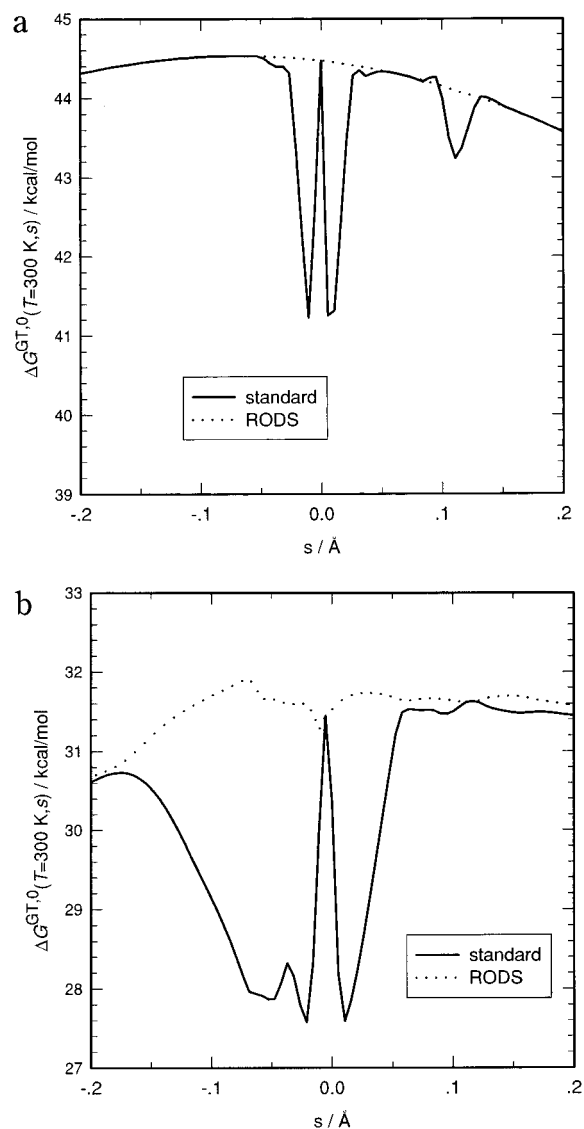


Figure 6. Detail of the generalized activation free energy curves at $T = 300 \text{ K}$ (in kcal mol⁻¹) versus the arc length along the reaction coordinate (in Å) for reactions R3 (a) and R4 (b). Solid lines correspond to the standard VTST calculation. Dotted lines correspond to the RODS VTST calculation.

the dip of the frequency). In the third zone, this generalized-normal-mode eigenvector becomes mainly a motion of the ammonia hydrogen atoms.

Frequency B in Figure 8 takes values close to 4000 cm⁻¹ from reactants up to the saddle point. Just at the saddle point, this frequency begins to decrease to values below 1500 cm⁻¹, and then it recovers rapidly to values around 4000 cm⁻¹. Its associated generalized-normal-mode eigenvector successively varies in the following way: first, it consists of the motion of the water hydrogen atoms; then, it involves the movement of the ammonia and W(N) water hydrogen atoms plus the N–C stretching; finally, it becomes essentially the motion of the W(N) water hydrogen atoms.

In summary, the frequency dips appear to be explained by spurious mixing of high-frequency motions into the reaction coordinate and the concomitant mixing of the heavy-atom motion along the reaction coordinate into transverse modes. This flattens the potential energy surface in the direction normal to the reaction coordinate.

3.2.2. Smaller Step Sizes. It is very hard to eliminate the spurious frequencies by simply decreasing the step sizes. For

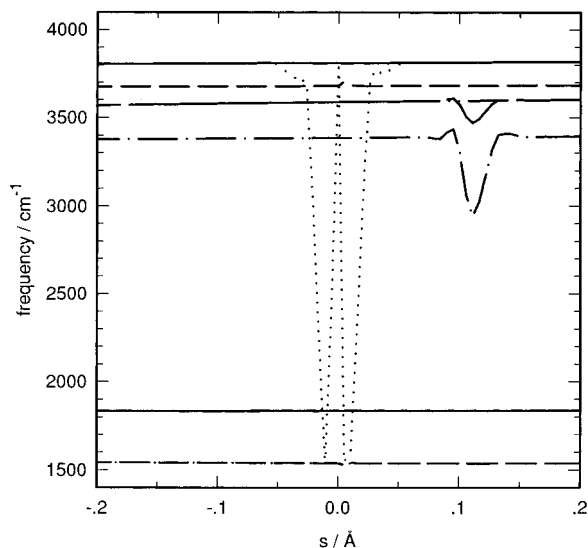


Figure 7. Diabatic generalized-normal-mode frequencies (in cm^{-1}) versus the arc length along the reaction coordinate (in \AA) along the reaction coordinate for the unhydrated reaction R3, based on the standard algorithm. Only frequencies correlated to reactant modes above 1500 cm^{-1} are displayed.

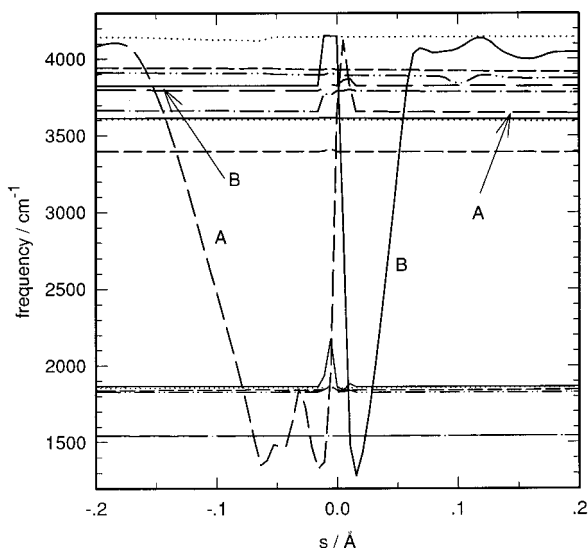


Figure 8. Diabatic generalized-normal-mode frequencies (in cm^{-1}) versus the arc length along the reaction coordinate (in \AA) along the reaction coordinate for the dihydrated reaction R4, based on the standard algorithm. Only frequencies correlated to reactant modes above 1500 cm^{-1} are displayed.

example, using the Euler algorithm and the ACESRATE code,³⁷ we decreased the step size for reaction R3 to $5.29 \times 10^{-4} \text{\AA}$. Although this somewhat decreases the oscillations, V_{MEP} is still not smooth, and V_a^G still shows a several kcal/mol dip. We therefore turn to the RODS algorithm, which we shall apply using the original 0.0026\AA step size data set that was generated with the Runge–Kutta algorithm implemented in GAMESS93.

3.3. VTST Calculations Based on the RODS Algorithm.

3.3.1. Adiabatic Potential Energy Curves and Free Energy of Activation Profiles. In the previous paper⁹ we showed that the RODS algorithm gave significant improvement in the stability of reaction-path calculations for the $\text{OH} + \text{H}_2$ and $\text{H} + \text{C}_2\text{H}_4$ reactions. The systems studied in the present paper pose more difficult challenges because the standard algorithm yields significant dips in the generalized frequency curves and, for this reason, also in the adiabatic ground-state potential energy

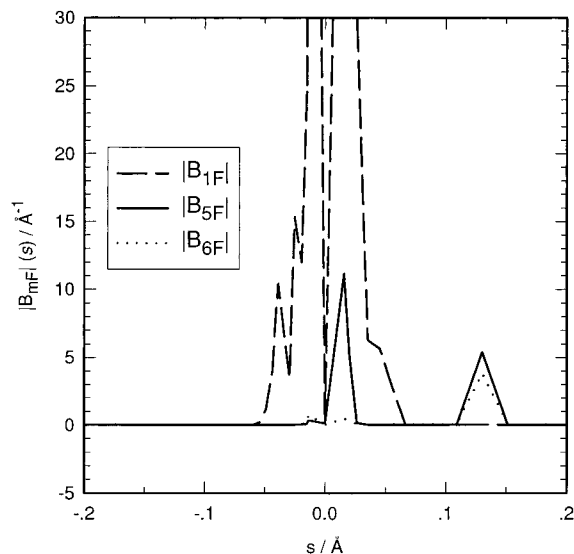


Figure 9. Absolute value of the reaction-path curvature components B_{mF} (in \AA^{-1}) versus the arc length along the reaction coordinate (in \AA) for modes 1, 5, and 6 for reaction R3.

curves and the corresponding free energy of activation profiles. Thus these reactions are good tests for the RODS algorithm.

The dips in the generalized-normal-mode frequencies disappear when the RODS algorithm is applied, and all the frequencies exhibit smooth behavior in the range of s considered in this paper. The frequencies obtained from the RODS algorithm do not suffer important crossings and are treated adiabatically. This translates into smooth vibrationally adiabatic ground-state potential energy curves, as shown by the dotted curves in parts a and b of Figure 5 for reactions R3 and R4, respectively. Analogously, dotted lines in parts a and b of Figure 6 show the free energy of activation profiles for R3 and R4 at 300 K. Note that the profile corresponding to reaction R4 is not very smooth, and this is attributable to the presence in this system of several low frequencies associated with the movements of water molecules. The use of a quadratic expansion of the potential on the dividing surface by the RODS algorithm⁹ may be quantitatively inadequate for those low frequencies and for their effect on the entropic term of the activation free energy.³⁵

3.3.2. Reaction-Path Curvature. Figures 9 and 10 show the absolute values of the highest reaction-path curvature components corresponding to reaction R3 and R4, respectively. These components have been calculated with eq 2, but using the direction normal to the RODS dividing surface instead of the gradient and with the RODS generalized-normal-mode eigenvectors. For reaction R3 we can distinguish two different regions. The first one, the region very close to the saddle point, has sharp peaks for frequency 1 and a lower peak for frequency 5 due to the interpolation needed in this region, where no electronic structure calculations have been done, because of the somewhat big initial step required in an MEP calculation. Apart from these central peaks, frequencies 5 and 6 in the R3 calculation have another peak at $s = 0.13 \text{\AA}$. This other peak causes the dip on those two frequencies in this region as shown in Figure 7.

Figure 10 shows the reaction-path curvature component for reaction R4 that corresponds to frequency 2, which has been adiabatically correlated along the path. This mode yields the only significant of the reaction-path curvature vector. This frequency includes the A and B motions discussed above, as shown in Figure 8. Again it is clear that the dips that appear in Figure 8 are caused by the strong coupling between the

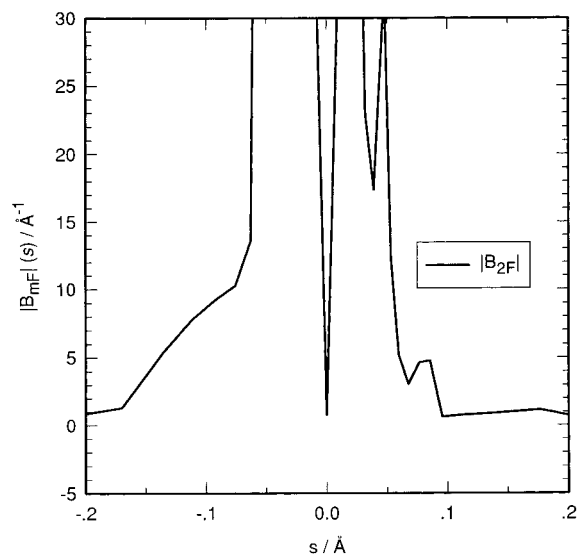


Figure 10. Absolute value of the reaction-path curvature components B_{mF} (in \AA^{-1}) versus the arc length along the reaction coordinate (in \AA) for mode 2 for reaction R3.

TABLE 3: Variational Transition State Location and Variational Effect on the Rate Constant for Reaction R3

T (K)	s_s^{CVT} (\AA)	$k^{\text{TST}}/k^{\text{CVT}}$	S_s^{CVT} (\AA)
200	-0.06	1.13	-0.02
300	-0.07	1.11	-0.03
400	-0.08	1.10	-0.03
600	-0.10	1.11	-0.04
800	-0.12	1.13	-0.05
1000	-0.14	1.15	-0.05

generalized normal mode eigenvectors associated with frequency 2 and the gradient.

We can rationalize the previous paragraphs in the following way. Let us suppose that a generalized normal mode \mathbf{L}_m is strongly coupled to the gradient at a given point on the MEP. If the reaction path is not followed precisely, a numerical bobsled effect will carry the calculated path into this direction. Sharp dips in generalized-normal-modes frequencies along the reaction path can then arise as a direct consequence of bobsledding out of the MEP, and this is, in turn, a consequence of the reaction-path curvature. The RODS algorithm is useful not only for eliminating the dips but also for analyzing the causes of those dips.

3.3.3. Canonical Variational Theory. Notice that in both Figures 5a and 6a the maximum values of the vibrationally adiabatic potential curves and the free energy of activation profiles occur very close to where they occurred in the conventional calculations without RODS, although one could not have had any confidence in the calculations without RODS, since the curves themselves were not globally converged. Figures 5b and 6b show more significant differences for reaction R4.

Let $s_s^{\text{CVT}}(T)$ denote the location of the variational transition state at temperature T . Table 3 gives s_s^{CVT} and the ratio of TST to CVT rate constants over a wide range of temperatures for reaction R3. One can see that the CVT transition state moves farther and farther toward reactants (i.e., toward negative s) as the temperature increases, and this produces a nonnegligible variational effect on the rate constant. However the quantitative effect is 15% or less over the entire temperature range in the table and is only 1.29 at 2000 K. One way to understand why the variational effect on the rate constant is small is to rescale the reaction coordinate in a more physical, system-specific way. Figure 1 shows that the transition vector is intermediate between

TABLE 4: Variational Transition State Location and Variational Effect on the Rate Constant for Reaction R4

T (K)	s_s^{CVT} (\AA)	$k^{\text{TST}}/k^{\text{CVT}}$	S_s^{CVT} (\AA)
200	-0.06	2.08	-0.02
300	-0.06	2.20	-0.02
400	-0.07	2.28	-0.02
600	-0.07	2.37	-0.02
800	-0.07	2.42	-0.02
1000	-0.07	2.45	-0.02

TABLE 5: Ground-State Transmission Coefficients To Account for Tunneling (RODS Calculation)

T (K)	reaction R3		reaction R4	
	ZCT	SCT	ZCT	SCT
200	2.09	3.34	2.10	17.6
300	1.35	1.66	1.34	3.48
400	1.18	1.32	1.17	2.03
600	1.08	1.13	1.07	1.38
800	1.04	1.07	1.04	1.20
1000	1.03	1.05	1.03	1.12

a pure motion of carbon and a relative motion of C primarily with respect to the three hydrogen atoms bonded to the nitrogen atom, whose motions would have reduced masses of 12 and 2.4 amu, respectively. Thus we rescaled the reaction coordinate to an intermediate value of 7 amu; this new reaction coordinate is called S . Table 3 shows that for this more physically scaled reaction coordinate the deviations of the variational transition state from the saddle point are only 0.02–0.05 \AA (0.11 \AA at 2000 K). Furthermore, the effective potential energy including zero-point contributions (i.e., the vibrationally adiabatic ground-state potential curve^{6,26}) is only 0.6 kcal/mol lower at the 2000 K transition state than at the 200 K one.

Table 4 lists the same variables as in Table 3 but corresponding now to the dihydrated reaction R4. The variational effects on the rate constants are much bigger for the dihydrated than for the unhydrated reaction, with TST overestimating the CVT result by a factor increasing from 2.08 at 200 K to 2.45 at 1000 K.

3.3.4. Tunneling Calculations. We did not present tunneling calculations in section 3.2 since Figure 5 shows that the adiabatic potential curves obtained without RODS are unphysical. Table 5 shows the ground-state transmission coefficients based on calculations in which we have implemented the RODS algorithm. For both ZCT and SCT calculations we evaluated $V_a^{\text{G}}(s)$ using the RODS frequencies. In addition to the shape of the effective potential energy curve, for the SCT calculations it is also necessary to compute the reaction-path curvature components. As explained above, we calculated these using the direction normal to the RODS dividing surface and the RODS values of the generalized-normal-mode eigenvectors.

For both reactions R3 and R4, the SCT values are significantly bigger than the ZCT ones. Since the ZCT transmission factors are based on tunneling along the MEP, while the SCT calculations account for corner cutting during tunneling, this result indicates that corner cutting of the tunneling path is important in this multidimensional reaction. A similar effect was observed in the $\text{S}_{\text{N}}2$ methyl exchange process between chloride and methyl chloride, where corner cutting of the tunneling path was attributed to the hydrogenic motions, but in that case the tunneling effect and corner cutting effect were both smaller. For example for reaction R1 at 300 K the ZCT transmission coefficients are 1.31 and 1.32 for $n = 0$ and 1, respectively, while the SCT transmission coefficients are 1.32 and 1.36.¹⁵ One reason for the larger effects in the present case is that the classical barriers with respect to reactants are much

TABLE 6: CVT/SCT Rate Constants (RODS Calculations)

T (K)	R3 ^a	R4 ^b
200	2.3 × 10 ⁷	1.1 × 10 ⁻⁴³
300	1.1 × 10 ⁹	3.2 × 10 ⁻³⁵
400	9.6 × 10 ⁹	6.1 × 10 ⁻³¹
600	1.0 × 10 ¹¹	1.5 × 10 ⁻²⁶
800	3.5 × 10 ¹¹	2.9 × 10 ⁻²⁴
1000	7.7 × 10 ¹¹	8.0 × 10 ⁻²³

^a In s⁻¹. ^b In cm³ molecule⁻¹ s⁻¹.

higher, 7.2 kcal for R3 and 20.5 kcal for R4, as compared to 3.1 kcal¹¹ and 4.8 kcal¹⁵ for R1 with $n = 0$ and 1, respectively. Even with these higher barriers, the values of the transmission factors obtained in this work for reactions R3 and R4 may seem surprisingly high, which is probably best interpreted by noting that Figures 1 and 3 show significant hydrogenic motions in the transition vectors. These hydrogenic motions are probably the dominant reason for the large tunneling effects. We note though that this is formally a heavy-atom tunneling effect (i.e., the dominant motion in the reaction coordinate is an atom heavier than H, D, or T), and significant tunneling of heavy-atom groups has also been observed in other theoretical calculations of organic reactions.³⁸

3.3.5. *Rate Constants.* The final rate constants are given in Table 6.

4. Conclusions

We have demonstrated that the RODS algorithm allows stable VTST and tunneling calculations on a new class of reactions that had proved intractable with earlier algorithms. The difficulty occurs when there are high-frequency modes strongly coupled to the reaction coordinate in a region where the energy is varying slowly along the reaction path, such as near the saddle point.

The RODS algorithm has also proved useful for accelerating convergence on a number of other problems.^{9,39} In the present case it showed its mettle on an even more intractable case. Its success in the present very difficult case is very encouraging for our ability to apply direct dynamics calculations to a wider variety of interesting applications in the future.

Finally we conclude that variational effects and tunneling effects can be significant for reactions involving methyl cation transfer when separated charge is created in the forward or reverse reaction.

Acknowledgment. The authors are grateful to Patton Fast for helpful discussions. This work was supported in part by the U.S. Department of Energy, Office of Basic Energy Sciences. Financial support from DGES (project No. PB95-0637) and the use of the computational facilities of the "Centre de Computació i de Comunicacions de Catalunya" are also gratefully acknowledged.

References and Notes

- (1) (a) Wigner, E. *Trans. Faraday Soc.* **1938**, *34*, 29. (b) Horiuti, J. *Bull. Chem. Soc. Jpn.* **1938**, *13*, 210.
- (2) Keck, J. C. *Adv. Chem. Phys.* **1967**, *13*, 85.
- (3) Garrett, B. C.; Truhlar, D. G. *J. Chem. Phys.* **1979**, *70*, 1593.
- (4) Garrett, B. C.; Truhlar, D. G. *Acc. Chem. Res.* **1980**, *13*, 440.
- (5) Garrett, B. C.; Truhlar, D. G. *J. Phys. Chem.* **1979**, *83*, 1079.
- (6) Garrett, B. C.; Truhlar, D. G.; Grev, R. S.; Magnuson, A. W. *J. Phys. Chem.* **1980**, *84*, 1730.

- (7) (a) Chatfield, D. C.; Friedman, R. S.; Truhlar, D. G.; Garrett, B. C.; Schwenke, D. W. *J. Am. Chem. Soc.* **1991**, *113*, 486. (b) Chatfield, D. C.; Friedman, R. S.; Schwenke, D. W.; Truhlar, D. G. *J. Phys. Chem.* **1992**, *96*, 2414. (c) Chatfield, D. C.; Friedman, R. S.; Mielke, S. L.; Schwenke, D. W.; Lynch, G. C.; Allison, T. C.; Truhlar, D. G. In *Dynamics of Molecules and Chemical Reactions*; Wyatt, R. E., Zhang, J. Z. H., Eds.; Marcel Dekker: New York, 1996; pp 323–386.
- (8) Melissas, V. S.; Truhlar, D. G.; Garrett, B. C. *J. Chem. Phys.* **1992**, *96*, 5758.
- (9) Villà, J.; Truhlar, D. G. *Theor. Chem. Acc.* **1997**, *97*, 317.
- (10) (a) Garrett, B. C.; Truhlar, D. G.; Grev, R. S. In *Potential Energy Surfaces and Dynamics Calculations*; Truhlar, D. G., Ed.; Plenum: New York, 1981; p 587. (b) Garrett, B. C.; Truhlar, D. G. *Annu. Rev. Phys. Chem.* **1984**, *35*, 159. (c) Truhlar, D. G.; Garrett, B. C. *J. Chim. Phys.* **1987**, *84*, 365. (d) Truhlar, D. G.; Garrett, B. C.; Klippenstein, S. J. *J. Phys. Chem.* **1996**, *100*, 12771.
- (11) Tucker, S. C.; Truhlar, D. G. *J. Am. Chem. Soc.* **1990**, *112*, 3347.
- (12) Zhao, X. G.; Tucker, S. C.; Truhlar, D. G. *J. Am. Chem. Soc.* **1991**, *113*, 826.
- (13) González-Lafont, A.; Truong, T. N.; Truhlar, D. G. *J. Phys. Chem.* **1991**, *95*, 4618.
- (14) Truhlar, D. G.; Lu, D.-h.; Tucker, S. C.; Zhao, X. G.; González-Lafont, A.; Truong, T. N.; Maurice, D.; Liu, Y.-P.; Lynch, G. C. *ACS Symp. Ser.* **1992**, *502*, 16.
- (15) Zhao, X. G.; Lu, D.-h.; Liu, Y.-P.; Lynch, G. C.; Truhlar, D. G. *J. Chem. Phys.* **1992**, *97*, 6369.
- (16) Viggiano, A. A.; Paschkewitz, J.; Morris, R. A.; Paulson, J. F.; González-Lafont, A.; Truhlar, D. G. *J. Am. Chem. Soc.* **1991**, *113*, 9404.
- (17) (a) Hu, W.-P.; Truhlar, D. G. *J. Am. Chem. Soc.* **1994**, *116*, 7797. (b) Hu, W.-P.; Truhlar, D. G. *J. Am. Chem. Soc.* **1995**, *117*, 10726.
- (18) Hu, W.-P.; Truhlar, D. G. *J. Am. Chem. Soc.* **1996**, *118*, 860.
- (19) (a) Gao, J. *J. Am. Chem. Soc.* **1991**, *113*, 7796. (b) Solà, M.; Lledós, A.; Duran, M.; Bertrán, J.; Abboud, J. L. M. *J. Am. Chem. Soc.* **1991**, *113*, 2873. (c) Gao, J.; Xinfu, X. *J. Am. Chem. Soc.* **1993**, *115*, 9667. (d) Gao, J.; Xinfu, X. *ACS Symp. Ser.* **1994**, *568*, 212. (e) Dillet, V.; Rinaldi, D.; Bertrán, J.; Rivail, J. L. *J. Chem. Phys.* **1996**, *104*, 9437.
- (20) Doubleday, C., Jr.; McIver, J. W., Jr.; Page, M. *J. Phys. Chem.* **1988**, *92*, 4367.
- (21) Baldrige, K. K.; Gordon, M. S.; Steckler, R.; Truhlar, D. G. *J. Phys. Chem.* **1989**, *93*, 5107.
- (22) Truhlar, D. G. In *The Reaction Path in Chemistry*; Heidrich, D., Ed.; Kluwer: Dordrecht, 1995; p 229.
- (23) Truong, T. N.; Duncan, W. T.; Bell, R. L. *ACS Symp. Ser.* **1996**, *629*, 85.
- (24) Szabo, A.; Ostlund, N. S. *Modern Quantum Chemistry*; Macmillan: New York, 1982.
- (25) Frisch, M. J.; Pople, J. A.; Binkley, J. S. *J. Chem. Phys.* **1984**, *80*, 3265.
- (26) Truhlar, D. G. Kupperman, A. *J. Am. Chem. Soc.* **1971**, *93*, 1840.
- (27) Truhlar, D. G.; Isaacson, A. D.; Garrett, B. C. In *Theory of Chemical Reaction Dynamics*; Baer, M., Ed.; CRC Press: Boca Raton, 1985; Vol. 4, p 65.
- (28) Mulliken, R. S. *J. Chem. Phys.* **1955**, *23*, 1833.
- (29) Schmidt, M. W.; Baldrige, K. K.; Boatz, J. A.; Elbert, S. T.; Gordon, M. S.; Jensen, J. H.; Koveki, S.; Matsunaga, N.; Nguyen, K. A.; Su, S.; Windus, T. L.; Elbert, S. T. *J. Comput. Chem.* **1993**, *14*, 1347.
- (30) Miller, W. H.; Handy, N. C.; Adams, J. E. *J. Chem. Phys.* **1980**, *72*, 99.
- (31) Lu, D.-h.; Truong, T. N.; Melissas, V. S.; Lynch, G. C.; Liu, Y.-P.; Garrett, B. C.; Steckler, R.; Isaacson, A. D.; Rai, S. N.; Hancock, G. C.; Lauderdale, J. G.; Joseph, T.; Truhlar, D. G. *Comput. Phys. Commun.* **1992**, *17*, 235.
- (32) Liu, Y.-P.; Lynch, G. C.; Truong, T. N.; Lu, D.-h.; Truhlar, D. G.; Garrett, B. C. *J. Am. Chem. Soc.* **1993**, *115*, 2408.
- (33) Steckler, R.; Chuang, Y.-Y.; Coitiño, E. L.; Hu, W.-P.; Liu, Y.-P.; Lynch, G. C.; Nguyen, K. A.; Jackels, C. F.; Gu, M. Z.; Rossi, I.; Fast, P.; Clayton, S.; Melissas, V. S.; Garrett, B. C.; Isaacson, A. D.; Truhlar, D. G. *POLYRATE*-version 7.0, University of Minnesota, Minneapolis, 1996.
- (34) Truhlar, D. G.; Isaacson, A. D. *J. Chem. Phys.* **1982**, *77*, 3516.
- (35) (a) Villà, J.; González-Lafont, A.; Lluch, J. M.; Bertrán, J. *Mol. Phys.* **1996**, *89*, 633. (b) Program *CORREL* can be downloaded from <http://klingon.uab.es/soft/theorchemsoft.html#correl>.
- (36) Truhlar, D. G.; Isaacson, A. D. *J. Chem. Phys.* **1991**, *94*, 357.
- (37) The *ACESRATE* program is described in Steckler, R.; Thurman, G. M.; Watts, J. D.; Bartlett, R. J. *J. Chem. Phys.* **1997**, *106*, 3926. The *ACESRATE* code is based on the *POLYRATE* dynamics code, in particular, Steckler, R.; Chuang, Y.-Y.; Coitiño, E. L.; Hu, W.-P.; Liu, Y.-P.; Lynch, G. C.; Nguyen, K. A.; Jackels, C. F.; Gu, M. Z.; Rossi, I.; Fast, P.; Clayton, S.; Melissas, V. S.; Garrett, B. C.; Isaacson, A. D.; Truhlar, D. G. *POLYRATE*-version 7.1, University of Minnesota, Minneapolis, February

1997, and on the ACES II electronic structure code, which is described in Stanton, J. F.; Gauss, J.; Watts, J. D.; Lauderdale, W. J.; Bartlett, R. T. *Int. J. Quantum Chem. Symp.* **1992**, *26*, 879.

(38) (a) Frei, H.; Pimentel, G. C. *J. Phys. Chem.* **1981**, *85*, 3355. (b) Carpenter, B. K. *J. Am. Chem. Soc.* **1983**, *105*, 1700. (c) Dewar, M. J. S.; Merz, K. M., Jr. *J. Phys. Chem.* **1985**, *89*, 4739. (d) Dewar, M. J. S.; Merz, K. M. *THEOCHEM* **1985**, *23*, 5. (e) Dewar, M. J. S.; Merz, K. M., Jr. *J. Am. Chem. Soc.* **1986**, *108*, 5634. (f) Sponsler, M. B.; Jain, R.; Coms, F. D.; Dougherty, D. A. *J. Am. Chem. Soc.* **1989**, *111*, 2240. (g) Zerbetto, F.;

Zgierski, M. Z.; Siebrand, W. *J. Am. Chem. Soc.* **1989**, *111*, 2799. (h) Zerbetto, F.; Zgierski, M. Z. *Chem. Phys.* **1989**, *130*, 4. (i) Arnold, B. R.; Radziszewski, J. G.; Campion, A.; Perry, S. S.; Michl, J. *J. Am. Chem. Soc.* **1991**, *113*, 692. (j) Orlandi, G.; Zerbetto, F. *Chem. Phys. Lett.* **1991**, *184*, 191. (k) Maier, G.; Wolf, R.; Kalinowski, H. O. *Angew. Chem., Int. Ed. Engl.* **1992**, *31*, 738. (l) Carsky, P.; Michl, J. *Theor. Chim. Acta* **1992**, *84*, 125. (m) Bosch, E.; Moreno, M.; Lluch, J. M. *J. Am. Chem. Soc.* **1992**, *114*, 2072.

(39) Fast, P. L.; Truhlar, D. G. Unpublished.